

AperTO - Archivio Istituzionale Open Access dell'Università di Torino

The Transiting Multi-planet System HD15337: Two Nearly Equal-mass Planets Straddling the Radius Gap

This is the author's manuscript

Original Citation:

Availability:

This version is available <http://hdl.handle.net/2318/1711523> since 2019-09-09T23:36:52Z

Published version:

DOI:10.3847/2041-8213/ab17d9

Terms of use:

Open Access

Anyone can freely access the full text of works made available as "Open Access". Works made available under a Creative Commons license can be used according to the terms and conditions of said license. Use of all other works requires consent of the right holder (author or publisher) if not exempted from copyright protection by the applicable law.

(Article begins on next page)

The transiting multi-planet system HD 15337: two nearly equal-mass planets straddling the radius gap

DAVIDE GANDOLFI,¹ LUCA FOSSATI,² JOHN H. LIVINGSTON,³ KEIVAN G. STASSUN,^{4,5} SASCHA GRZIWA,⁶
OSCAR BARRAGÁN,⁷ MALCOLM FRIDLUND,^{8,9} DARIA KUBYSHKINA,² CARINA M. PERSSON,⁸ FEI DAI,^{10,11}
KRISTINE W. F. LAM,¹² SIMON ALBRECHT,¹³ NATALIE BATALHA,¹⁴ PAUL G. BECK,^{15,16} ANDERS BO JUSTESEN,¹³
JUAN CABRERA,¹⁷ SCOTT CARTWRIGHT,¹⁸ WILLIAM D. COCHRAN,¹⁹ SZILARD CSIZMADIA,¹⁷ MISTY D. DAVIES,²⁰
HANS J. DEEG,^{15,16} PHILIPP EIGMÜLLER,¹⁷ MICHAEL ENDL,¹⁹ ANDERS ERIKSON,¹⁷ MASSIMILIANO ESPOSITO,²¹
RAFAEL A. GARCÍA,²² ROBERT GOEKE,¹⁰ LUCÍA GONZÁLEZ-CUESTA,^{15,16} EIKE W. GUENTHER,²¹ ARTIE P. HATZES,²¹
DIEGO HIDALGO,¹⁵ TERUYUKI HIRANO,²³ MARIA HJORTH,¹³ PETR KABATH,²⁴ EMIL KNUDSTRUP,¹³ JUDITH KORTH,⁶
JIE LI,²⁵ RAFAEL LUQUE,^{15,16} SAVITA MATHUR,^{15,16} PILAR MONTAÑES RODRÍGUEZ,^{15,16} NORIO NARITA,^{3,15,26,27,28}
DAVID NESPRAL,^{15,16} PRAJWAL NIRLA,²⁹ GRZEGORZ NOWAK,^{15,16} ENRIC PALLE,^{15,16} MARTIN PÄTZOLD,⁶
JORGE PRIETO-ARRANZ,^{15,16} HEIKE RAUER,^{12,17,30} SETH REDFIELD,³¹ IGNASI RIBAS,^{32,33} MAREK SKARKA,^{24,34}
ALEXIS M. S. SMITH,¹⁷ PAMELA ROWDEN,³⁵ GUILLERMO TORRES,³⁶ VINCENT VAN EYLEN,¹¹ AND MICHAEL L. VEZIE¹⁰

¹*Dipartimento di Fisica, Università degli Studi di Torino, via Pietro Giuria 1, I-10125, Torino, Italy*

²*Space Research Institute, Austrian Academy of Sciences, Schmiedlstrasse 6, A-8041 Graz, Austria*

³*Department of Astronomy, University of Tokyo, 7-3-1 Hongo, Bunkyo-ku, Tokyo 113-0033, Japan*

⁴*Vanderbilt University, Department of Physics & Astronomy, 6301 Stevenson Center Ln., Nashville, TN 37235, US*

⁵*Fisk University, Department of Physics, 1000 17th Ave. N., Nashville, TN 37208, US*

⁶*Rheinisches Institut für Umweltforschung an der Universität zu Köln, Aachener Strasse 209, 50931 Köln, Germany*

⁷*Oxford Astrophysics, Department of Physics, University of Oxford, Denys Wilkinson Building, Keble Road, Oxford, OX1 3RH, UK*

⁸*Department of Space, Earth and Environment, Chalmers University of Technology, Onsala Space Observatory, 439 92 Onsala, Sweden*

⁹*Leiden Observatory, University of Leiden, PO Box 9513, 2300 RA, Leiden, The Netherlands*

¹⁰*Department of Physics and Kavli Institute for Astrophysics and Space Research, MIT, Cambridge, MA 02139, USA*

¹¹*Department of Astrophysical Sciences, Princeton University, 4 Ivy Lane, Princeton, NJ, 08544, USA*

¹²*Center for Astronomy and Astrophysics, TU Berlin, Hardenbergstr. 36, 10623 Berlin, Germany*

¹³*Stellar Astrophysics Centre, Dep. of Physics and Astronomy, Aarhus University, Ny Munkegade 120, DK-8000 Aarhus C, Denmark*

¹⁴*Department of Astronomy and Astrophysics, University of California, Santa Cruz, CA 95064, USA*

¹⁵*Instituto de Astrofísica de Canarias, C/ Vía Láctea s/n, 38205 La Laguna, Spain*

¹⁶*Departamento de Astrofísica, Universidad de La Laguna, 38206 La Laguna, Spain*

¹⁷*Institute of Planetary Research, German Aerospace Center, Rutherfordstrasse 2, 12489 Berlin, Germany*

¹⁸*Proto-Logic LLC, 1718 Euclid Street NW, Washington, DC 20009, USA*

¹⁹*Department of Astronomy and McDonald Observatory, University of Texas at Austin, 2515
Speedway, Stop C1400, Austin, TX 78712, USA*

²⁰*NASA Ames Research Center, Moffett Field, CA 94035, USA*

²¹*Thüringer Landessternwarte Tautenburg, Sternwarte 5, D-07778 Tautenburg, Germany*

²²*Laboratoire AIM, CEA/DSM – CNRS – Univ. Paris Diderot - IRFU/SAP, Centre de Saclay, 91191 Gif-sur-Yvette, France*

²³*Department of Earth and Planetary Sciences, Tokyo Institute of Technology, 2-12-1 Ookayama, Meguro-ku, Tokyo 152-8551, Japan*

²⁴*Astronomical Institute, Czech Academy of Sciences, Fričova 298, 25165, Ondřejov, Czech Republic*

²⁵*Aerospace Computing Inc./NASA Ames Research Center, Moffett Field, CA 94035, USA*

²⁶*Astrobiology Center, NINS, 2-21-1 Osawa, Mitaka, Tokyo 181-8588, Japan*

²⁷*National Astronomical Observatory of Japan, NINS, 2-21-1 Osawa, Mitaka, Tokyo 181-8588, Japan*

²⁸*JST, PRESTO, 7-3-1 Hongo, Bunkyo-ku, Tokyo 113-0033, Japan*

²⁹*Department of Earth, Atmospheric and Planetary Sciences, Massachusetts Institute of Technology, Cambridge, MA 02139*

³⁰*Institute of Geological Sciences, FU Berlin, Malteserstr. 74-100, D-12249 Berlin*

³¹*Astronomy Department and Van Vleck Observatory, Wesleyan University, Middletown, CT 06459, USA*

³²*Institut de Ciències de l'Espai (ICE, CSIC), Campus UAB, C/ de Can Magrans s/n, E-08193 Bellaterra, Spain*

³³*Institut d'Estudis Espacials de Catalunya (IEEC), C/ Gran Capità 2-4, E-08034 Barcelona, Spain*

³⁴*Department of Theoretical Physics and Astrophysics, Masaryk University, Kotlářská 2, 61137 Brno, Czech Republic*

³⁵*School of Physical Sciences, The Open University, Walton Hall, Milton Keynes MK7 6AA, United Kingdom*

³⁶*Center for Astrophysics | Harvard & Smithsonian, 60 Garden Street, Cambridge, MA 02138, USA*

(Received March 13, 2019; Revised March 28, 2019; Accepted April 2, 2019)

ABSTRACT

We report the discovery of a super-Earth and a sub-Neptune transiting the star HD 15337 (TOI-402, TIC 120896927), a bright ($V=9$) K1 dwarf observed by the *Transiting Exoplanet Survey Satellite* (*TESS*) in Sectors 3 and 4. We combine the *TESS* photometry with archival HARPS spectra to confirm the planetary nature of the transit signals and derive the masses of the two transiting planets. With an orbital period of 4.8 days, a mass of $7.51^{+1.09}_{-1.01} M_{\oplus}$, and a radius of $1.64 \pm 0.06 R_{\oplus}$, HD 15337 b joins the growing group of short-period super-Earths known to have a rocky terrestrial composition. The sub-Neptune HD 15337 c has an orbital period of 17.2 days, a mass of $8.11^{+1.82}_{-1.69} M_{\oplus}$, and a radius of $2.39 \pm 0.12 R_{\oplus}$, suggesting that the planet might be surrounded by a thick atmospheric envelope. The two planets have similar masses and lie on opposite sides of the radius gap, and are thus an excellent testbed for planet formation and evolution theories. Assuming that HD 15337 c hosts a hydrogen-dominated envelope, we employ a recently developed planet atmospheric evolution algorithm in a Bayesian framework to estimate the history of the high-energy (extreme ultraviolet and X-ray) emission of the host star. We find that at an age of 150 Myr, the star possessed on average between 3.7 and 127 times the high-energy luminosity of the current Sun.

Keywords: Planetary systems – Planets and satellites: individual: HD 15337 b and c – Stars: fundamental parameters – Stars: individual: HD 15337 – Techniques: photometric – Techniques: radial velocities

1. INTRODUCTION

Successfully launched in April 2018, NASA’s *Transiting Exoplanet Survey Satellite* (*TESS*) is making a significant step forward in understanding the diversity of exoplanets, and especially of super-Earths ($R_p = 1\text{--}2 R_{\oplus}$) and sub-Neptunes ($R_p = 2\text{--}4 R_{\oplus}$). *TESS* is performing an all-sky photometric search for planets transiting bright stars ($6 < V < 11$), so that detailed characterizations of the planets and their atmospheres can be performed (Ricker et al. 2015). The survey is broken up into 26 sectors – each sector being observed for ~ 28 days and consisting of four cameras with a combined field of view of $24^\circ \times 96^\circ$. Candidate alerts and full-frame images are released every month. As of March 2019, *TESS* has already announced the discovery of about a dozen transiting planets (see, e.g., Esposito et al. 2019; Gandolfi et al. 2018; Huang et al. 2018; Jones et al. 2018; Nielsen et al. 2019; Quinn et al. 2019; Trifonov et al. 2019).

TESS has already led to the detection of “golden” systems amenable to in-depth characterization of planetary atmospheres, such as π Men, which is a bright ($V=5.65$) star hosting a transiting super-Earth with a bulk density that is consistent with either a primary, hydrogen-dominated atmosphere, or a secondary, probably $\text{CO}_2/\text{H}_2\text{O}$ -dominated, atmosphere (Gandolfi et al. 2018; Huang et al. 2018). The discovery of such systems is central for studying planetary atmospheres via multi-wavelength transmission spectroscopy, and for constraining the evolution models of planetary atmospheres.

TESS also enables the discovery of multi-planet systems for which both mass and radius can be precisely measured. Because such planets orbit the same star, differences in mean density and atmospheric structure among planets belonging to the same system can be ascribed mainly to differences in planetary mass and orbital separation (see, e.g., Guenther et al. 2017; Prieto-Arranz et al. 2018). This greatly simplifies modeling of their past evolution history, thus constraining how these planets formed (Alibert et al. 2005; Alibert & Benz 2017). In this respect, even more significant are multi-planet systems in which two or more planets have similar masses, as differences in radii would most likely be due to the different orbital separations.

In this Letter we report the discovery of two small planets transiting the bright ($V=9$) star HD 15337 (Table 1), a K1 dwarf observed by *TESS* in Sectors 3 and 4. We combined the *TESS* photometry with archival HARPS radial velocities (RVs) to confirm the planetary nature of the transit signals and derive the masses of the two planets. This Letter is organized as follows. In Sect. 2, we describe the *TESS* photometry and the detection of the transit signals. In Sect. 3, we present the archival HARPS spectra. The properties of the host star are reported in Sect. 4. We present the frequency analysis of the HARPS RVs in Sect. 5 and the data modeling in Sect. 6. Results, discussions, and a summary are given in Sect. 7.

Table 1. Main identifiers, coordinates, proper motion, parallax, distance, and optical and infrared magnitudes of HD 15337.

Parameter	Value	Source
<i>Main Identifiers</i>		
HD	15337	
HIP	11433	<i>Hipparcos</i>
TIC	120896927	TIC ^a
TOI	402	<i>TESS</i> Alerts
<i>Gaia</i> DR2	5068777809824976256	<i>Gaia</i> DR2 ^b
<i>Equatorial Coordinates</i>		
R.A. (J2000.0)	02 ^h 27 ^m 28.3781 ^s	<i>Gaia</i> DR2 ^b
Decl. (J2000.0)	−27° 38′ 06.7417″	<i>Gaia</i> DR2 ^b
<i>Proper Motion, Parallax, and Distance</i>		
$\mu_\alpha \cos \delta$ (mas yr ^{−1})	−73.590 ± 0.057	<i>Gaia</i> DR2 ^b
μ_δ (mas yr ^{−1})	−211.614 ± 0.082	<i>Gaia</i> DR2 ^b
Parallax (mas)	22.285 ± 0.035	<i>Gaia</i> DR2 ^b
Distance (pc)	44.874 ± 0.070	<i>Gaia</i> DR2 ^b
<i>Magnitudes</i>		
B_T	10.170 ± 0.027	<i>Tycho-2</i> ^c
V_T	9.184 ± 0.018	<i>Tycho-2</i> ^c
B	10.009 ± 0.090	APASS ^d
V	9.096 ± 0.017	APASS ^d
g	9.852 ± 0.493	APASS ^d
r	8.847 ± 0.016	APASS ^d
i	8.655 ± 0.054	APASS ^d
u	11.756 ± 0.075	Strömgren ^e
v	10.526 ± 0.046	Strömgren ^e
b	9.598 ± 0.032	Strömgren ^e
y	9.088 ± 0.030	Strömgren ^e
G	8.8560 ± 0.0002	<i>Gaia</i> DR2 ^b
G_{BP}	9.3194 ± 0.0011	<i>Gaia</i> DR2 ^b
G_{RP}	8.2708 ± 0.0016	<i>Gaia</i> DR2 ^b
J	7.553 ± 0.019	2MASS ^f
H	7.215 ± 0.034	2MASS ^f
K_s	7.044 ± 0.018	2MASS ^f
$W1(3.35 \mu\text{m})$	6.918 ± 0.054	ALLWISE ^g
$W2(4.6 \mu\text{m})$	7.048 ± 0.020	ALLWISE ^g
$W3(11.6 \mu\text{m})$	7.015 ± 0.017	ALLWISE ^g
$W4(22.1 \mu\text{m})$	6.916 ± 0.072	ALLWISE ^g

NOTE—(a) *TESS* Input Catalog (TIC; [Stassun et al. 2018b](#)); (b) *Gaia* Data Release 2 (DR2; [Gaia Collaboration et al. 2018](#)); (c) *Tycho-2* catalog ([Høg et al. 2000](#)); (d) AAVSO Photometric All-Sky Survey (APASS; [Henden et al. 2015](#)); (e) Strömgren-Crawford $uvby\beta$ photometry catalog ([Paunzen 2015](#)); (f) Two-micron All Sky Survey (2MASS; [Cutri et al. 2003](#)); (g) Wide-field Infrared Survey Explorer catalog (WISE; [Cutri 2013](#)).

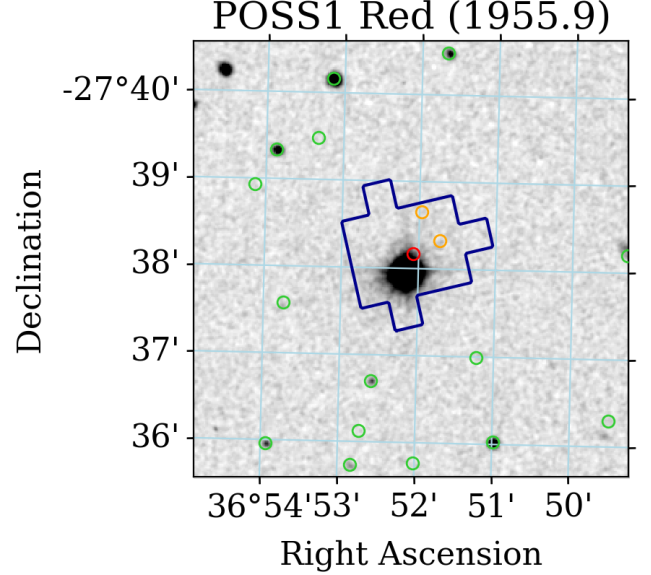


Figure 1. 5′ × 5′ 103aE emulsion image taken in 1955 from the First Palomar Sky Survey (POSS1-E), with the Sector 4 SPOC photometric aperture overplotted in blue (*TESS* pixel size is 21″), and the positions of *Gaia* DR2 sources (J2015.5) within 2′ of HD 15337 indicated by circles. HD 15337 is in red, nearby sources contributing more than 1% of their flux to the aperture are in orange, and other sources are in green; the Sector 3 aperture is slightly bigger but yields similarly low levels of photometric dilution

(see Sect. 2). Due to the proper motion of HD 15337, there is a $\sim 14''$ offset between its *Gaia* position and its position in the image.

2. *TESS* PHOTOMETRY

HD 15337 (TIC 120896927) was observed by *TESS* Camera #2 in Sectors 3 and 4 (charge-coupled devices #3 and #4, respectively) from 20 September 2018 to 15 November 2018, and will not be observed further during the nominal two-year *TESS* mission. Photometry was interrupted when the satellite was re-pointed for data downlink, from $\text{BJD}_{\text{TDB}} = 2458395.4$ to $\text{BJD}_{\text{TDB}} = 2458396.6$ in Sector 3, and from $\text{BJD}_{\text{TDB}} = 2458423.5$ to $\text{BJD}_{\text{TDB}} = 2458424.6$ in Sector 4. There is an additional data gap in Sector 4 from $\text{BJD}_{\text{TDB}} = 2458418.5$ to $\text{BJD}_{\text{TDB}} = 2458421.2$, which was caused by an interruption in communications between the instrument and spacecraft.

TESS objects of interest (TOIs) are announced publicly via the *TESS* data alerts web portal¹ at the Massachusetts Institute of Technology. TOIs 402.01 (HD 15337 b) and 402.02 (HD 15337 c) were announced on 16 January 2019 and 31 January 2019, respectively, in

¹ <https://tess.mit.edu/alerts>.

association with the HD 15337 photometry. The *TESS* pixel data and light curves produced by the Science Processing Operations Center (SPOC; Jenkins et al. 2016) at NASA Ames Research Center were subsequently made publicly available via the Mikulski Archive for Space Telescopes (MAST).² We iteratively searched the SPOC light curves for transit signals using the Box-least-squares algorithm (BLS; Kovács et al. 2002), after fitting and removing stellar variability using a cubic spline with knots every 1.0 day. We recovered two signals corresponding to the TOIs, but no other significant signals were detected. We also tried removing variability using the wavelet-based filter routines VARLET and PHALET, but it did not change the BLS results; we are thus confident that the two signals are robustly detected and are not the result of data artifacts resulting from the choice of variability model or residual instrumental systematic signals.

The SPOC light curves are produced using automatically selected optimal photometric apertures. We also produced light curves from the *TESS* pixel data using a series of apertures (Gandolfi et al. 2018; Esposito et al. 2019), and found that apertures larger than the SPOC aperture shown in Fig. 1 minimized the 6.5 hr combined differential photometric precision (CDPP) noise metric (Christiansen et al. 2012). However, the transit signals recovered from these light curves were slightly less significant, which we attributed to the improvement in light curve quality afforded by the Presearch Data Conditioning (Smith et al. 2012; Stumpe et al. 2012) pipeline used by the SPOC, which corrects for common-mode systematic noise; for this reason, we opted to analyze the SPOC light curves for the remainder of the analysis in this Letter.

To investigate the possibility of diluting flux from stars other than HD 15337, we visually inspected archival images and compared *Gaia* DR2 (Gaia Collaboration et al. 2018) source positions with the SPOC photometric apertures. We used the coordinates of HD 15337 from the *TESS* Input Catalog³ (Stassun et al. 2018b) to retrieve *Gaia* DR2 sources using a search radius of 3'. In an archival image taken in 1955 from the Firs Palomar Sky Survey (POSSI-E)⁴, HD 15337 is offset from its current position by $\sim 14''$ due to proper motion, but this is not sufficient to completely rule out chance alignment with a background source; however, such an alignment with a bright source is highly unlikely. Assuming

the *TESS* point spread function (PSF) can be approximated by a two-dimensional Gaussian profile with a full-width at half maximum (FWHM) of $\sim 25''$, we found that 98.9% (98.5%) of the flux from HD 15337 is within the Sector 3 (Sector 4) SPOC aperture. Approximating the *TESS* bandpass with the *Gaia* G_{RP} bandpass, the transit signals from HD 15337 should be diluted by less than 0.01% in both apertures; HD 15337 is the only star bright enough to be the source of the transit signals. Two other *Gaia* DR2 sources (5068777809825770112 and 5068777745400963584) also contribute flux, but they are too faint to yield significant dilution ($G_{\text{RP}} \approx 19$ mag). Fig. 1 shows the archival image, along with *Gaia* DR2 source positions and the Sector 4 SPOC photometric aperture.

3. HARPS SPECTROSCOPIC OBSERVATIONS

HD 15337 was observed between 15 December 2003 and 06 September 2017 UT with the High Accuracy Radial velocity Planet Searcher (HARPS) spectrograph ($R \approx 115\,000$, Mayor et al. 2003) mounted at the ESO-3.6 m telescope, as part of the observing programs 072.C-0488, 183.C-0972, 192.C-0852, 196.C-1006, and 198.C-0836. We retrieved the publicly available reduced spectra from the ESO archive, along with the cross-correlation function (CCF) and its bisector, computed from the dedicated HARPS pipeline using a K5 numerical mask (Baranne et al. 1996). On June 2015, the HARPS fiber bundle was upgraded and a new set of octagonal fibers, with improved mode-scrambling capabilities, were installed (Lo Curto et al. 2015). To account for the RV offset caused by the instrument refurbishment, we treated the HARPS RVs taken before/after June 2015 as two different data sets. Tables 3 and 4 list the HARPS RVs taken with the old and new fiber bundle, along with the RV uncertainties, the full-width at half maximum (FWHM) and bisector span (BIS) of the CCF, the exposure times, and the signal-to-noise ratio (S/N) per pixel at 5500 Å. Time stamps are given in barycentric Julian Date in the barycentric dynamical time (BJD_{TDB}). We rejected two data points – marked with asterisks in Tables 3 and 4 – because of poor S/N ratio ($\text{BJD}_{\text{TDB}} = 2455246.519846$) or systematics ($\text{BJD}_{\text{TDB}} = 2457641.794439$).

4. STELLAR FUNDAMENTAL PARAMETERS

4.1. Spectroscopic parameters

We co-added the HARPS spectra obtained with the old and new fiber bundle separately to get two combined spectra with S/N per pixel at 5500 Å of 590 (old fiber) and 490 (new fiber). We derived the spectroscopic parameters of HD 15337 from the co-added

² <https://mast.stsci.edu>.

³ Available at <https://mast.stsci.edu/portal/Mashup/Clients/Mast/Portal.html>.

⁴ Available at http://archive.stsci.edu/cgi-bin/dss_form.

HARPS spectra using Spectroscopy Made Easy (SME), a spectral analysis tool that calculates synthetic spectra and fits them to high-resolution observed spectra using a χ^2 minimizing procedure. The analysis was performed with the non-local thermodynamic equilibrium (non-LTE) SME version 5.2.2, along with MARCS model atmospheres (Gustafsson et al. 2008).

We estimated a microturbulent velocity of $v_{\text{mic}} = 0.80 \pm 0.10 \text{ km s}^{-1}$ from the empirical calibration equations for Sun-like stars from Bruntt et al. (2010). The effective temperature T_{eff} was measured fitting the wings of the H_α and H_β lines, as well as the Na I doublet at 5890 and 5896 Å (Fuhrmann et al. 1993; Axer et al. 1994; Fuhrmann et al. 1994, 1997b,a). The surface gravity $\log g_*$ was determined from the wings of the Ca I $\lambda 6102$, $\lambda 6122$, $\lambda 6162$ Å triplet, and the Ca I $\lambda 6439$ Å line, as well as from the Mg I $\lambda 5167$, $\lambda 5173$, $\lambda 5184$ Å triplet. We measured the iron abundance $[\text{Fe}/\text{H}]$, the macroturbulent velocity v_{mac} , and the projected rotational velocity $v \sin i_*$ by simultaneously fitting the unblended iron lines in the spectral region 5880–6600 Å.

Our analyses applied to the two stacked HARPS spectra provided consistent results, well within the uncertainties. The final adopted values are listed in Table 2. We derived an effective temperature of $T_{\text{eff}} = 5125 \pm 50 \text{ K}$, surface gravity $\log g_* = 4.40 \pm 0.10$ (cgs), and an iron abundance relative to solar of $[\text{Fe}/\text{H}] = 0.15 \pm 0.08$ dex. We also measured a calcium abundance of $[\text{Ca}/\text{H}] = 0.16 \pm 0.05$ dex and a sodium abundance of $[\text{Na}/\text{H}] = 0.27 \pm 0.09$ dex. We found a macroturbulent velocity of $v_{\text{mac}} = 3.0 \pm 1.0 \text{ km/s}$ in agreement with the value predicted from the empirical equations of Doyle et al. (2014). The projected rotational velocity was found to be $v \sin i_* = 1.0 \pm 1.0 \text{ km s}^{-1}$.

4.2. Stellar mass, radius, age and interstellar extinction

We performed an analysis of the broadband spectral energy distribution (SED) together with the *Gaia* Data Release 2 (DR2; Gaia Collaboration et al. 2018) parallax in order to determine an empirical measurement of the stellar radius, following the procedures described in Stassun & Torres (2016), Stassun et al. (2017), and Stassun et al. (2018a). We retrieved the B_T and V_T magnitudes from *Tycho-2* catalog (Høg et al. 2000), the Strömgren *ubvy* magnitudes from Paunzen (2015), the *BVgri* magnitudes from APASS (Henden et al. 2015), the *JHK_S* magnitudes from 2MASS (Cutri et al. 2003), the *W1–W4* magnitudes from *ALLWISE* (Cutri 2013), and the *G* magnitude from *Gaia* DR2 (Gaia Collaboration et al. 2018). Together, the available photometry spans the full stellar SED over the wavelength

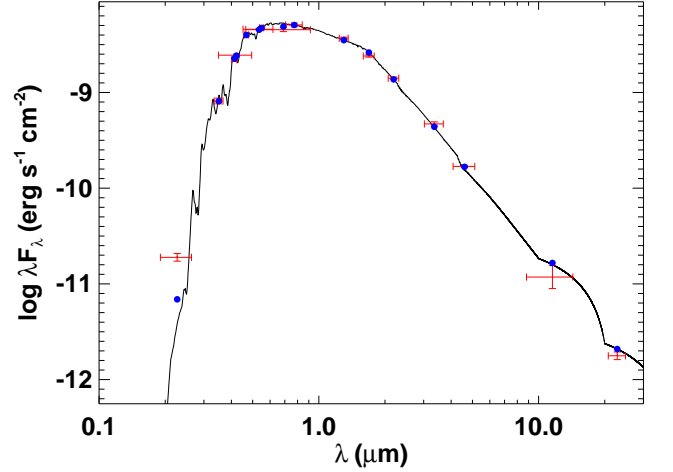


Figure 2. Spectral energy distribution (SED) of HD 15337. Red symbols represent the observed photometric measurements, where the horizontal bars represent the effective width of the passband. Blue symbols are the model fluxes from the best-fit Kurucz atmosphere model (black).

range 0.35–22 μm (Table 1 and Fig. 2). In addition, we retrieved the near-ultraviolet (NUV) flux from the *Galaxy Evolution Explorer* (*GALEX*) survey (Bianchi et al. 2011) in order to assess the level of chromospheric activity, if any.

We performed a fit using Kurucz stellar atmosphere models (Castelli & Kurucz 2003), with the fitted parameters being the effective temperature T_{eff} and iron abundance $[\text{Fe}/\text{H}]$, as well as the interstellar extinction A_V , which we restricted to the maximum line-of-sight value from the dust maps of Schlegel et al. (1998). The broadband SED is largely insensitive to the surface gravity ($\log g_*$), thus we simply adopted the value from the initial spectroscopic analysis presented in the previous subsection. The resulting fit (Fig. 2) gives a reduced χ^2 of 2.3 (excluding the *GALEX* NUV flux, which is consistent with a modest level of chromospheric activity). The best-fitting effective temperature and iron content are $T_{\text{eff}} = 5130 \pm 50 \text{ K}$ and $[\text{Fe}/\text{H}] = 0.1^{+0.2}_{-0.1}$ dex, respectively, in excellent agreement with the spectroscopic values (Sect. 4.1 and Table 2). We found that the reddening of HD 15337 is consistent with zero ($A_V = 0.02 \pm 0.02$ mag), as expected given the relatively short distance to the star ($\sim 45 \text{ pc}$). Integrating the unreddened model SED gives a bolometric flux at Earth of $F_{\text{bol}} = 7.29 \pm 0.08 \times 10^{-9} \text{ erg s cm}^{-2}$. Taking the F_{bol} and T_{eff} together with the *Gaia* DR2 parallax, adjusted by +0.08 mas to account for the systematic offset reported by Stassun & Torres (2018), gives the stellar radius as $R_* = 0.856 \pm 0.017 R_\odot$. Finally, estimating the stellar mass from the empirical relations of Torres et al. (2010) and a 6% error

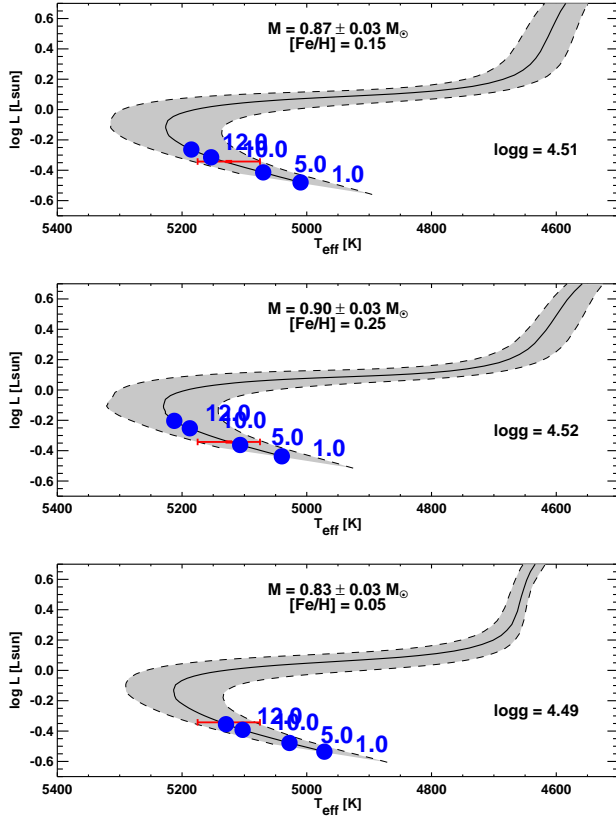


Figure 3. Hertzsprung–Russell Diagram for HD 15337 based on the observed effective temperature and bolometric luminosity, the latter computed directly from F_{bol} and the *Gaia* parallax-based distance. Each panel compares the observed properties of the star to evolutionary tracks from the Yonsei–Yale models (Yi et al. 2001; Spada et al. 2013) for different permitted combinations of stellar mass and metallicity. Blue points with labels represent the model ages in Gyr. The central panel represents the case most compatible with all of the available data, including the stellar age of ≈ 5.1 Gyr as determined from the observed chromospheric activity and stellar rotation period (see the text).

from the empirical relation itself gives a stellar mass of $M_{\star} = 0.91 \pm 0.06 M_{\odot}$.

We can refine the stellar mass estimate by taking advantage of the observed chromospheric activity, which can constrain the age of the star via empirical relations. For example, taking the chromospheric activity indicator, $\log R'_{\text{HK}} = -4.916 \pm 0.038$ from Gomes da Silva et al. (2014) and applying the empirical relations of Mamajek & Hillenbrand (2008), gives a predicted age of 5.1 ± 0.8 Gyr. As shown in Fig. 3, according to the Yonsei–Yale stellar evolutionary models (Yi et al. 2001; Spada et al. 2013), this age is most compatible with a stellar mass of $M_{\star} = 0.90 \pm 0.03 M_{\odot}$ and $[\text{Fe}/\text{H}] = 0.25$ dex, which with the empirically deter-

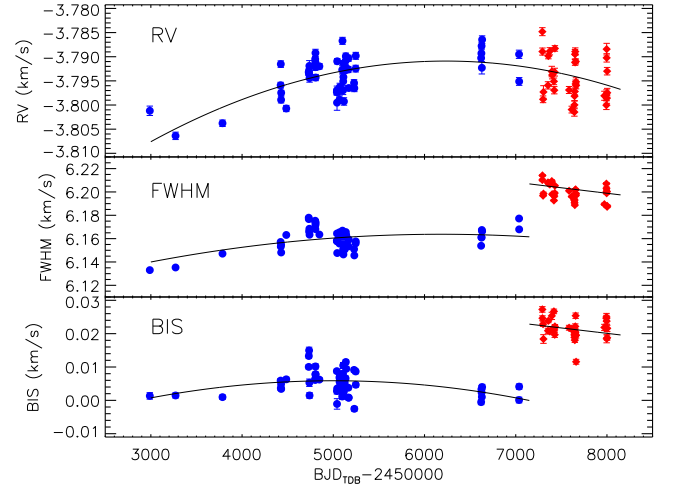


Figure 4. Offset-corrected HARPS RVs of HD 15337 (upper panel), and FWHM and BIS of the cross-correlation function (middle and lower panels). The blue circles and red diamonds mark the measurements acquired with the old and new fiber bundle, respectively. The thick lines mark the best-fitting parabolic curves to the data (see the text).

mined stellar radius implies a stellar $\log g_{\star} = 4.53 \pm 0.02$ (cgs) – in good agreement with the spectroscopic value of $\log g_{\star} = 4.40 \pm 0.10$ (cgs).

Other combinations of stellar mass and metallicity are compatible with the observed effective temperature and radius (Fig. 3); however they require ages that are incompatible with that predicted by the chromospheric R'_{HK} emission. Finally, we can further corroborate the activity-based age estimate by also using empirical relations to predict the stellar rotation period from the activity. For example, the empirical relation between R'_{HK} and rotation period from Mamajek & Hillenbrand (2008) predicts a rotation period for this star of ≈ 42 days, which is compatible with the observed rotation period derived from the HARPS RVs and activity indicators ($P_{\text{rot}} = 36.5$ days; see the following section).

5. FREQUENCY ANALYSIS OF THE HARPS MEASUREMENTS

We performed a frequency analysis of the HARPS time-series to search for the Doppler reflex motion induced by the two transiting planets discovered by *TESS*. We accounted for the RV offset between the two different set-ups of the instrument (old and new fiber bundle) using the value of 19.7 m s^{-1} derived from the joint analysis presented in Sect. 6, which is in good agreement with the expected offset for a slowly rotating K1 V star such as HD 15337 (Lo Curto et al. 2015).

The offset-corrected HARPS RVs are displayed in Fig. 4 (upper panel), along with the time-series of the full-width at half maximum (FWHM; middle panel) and

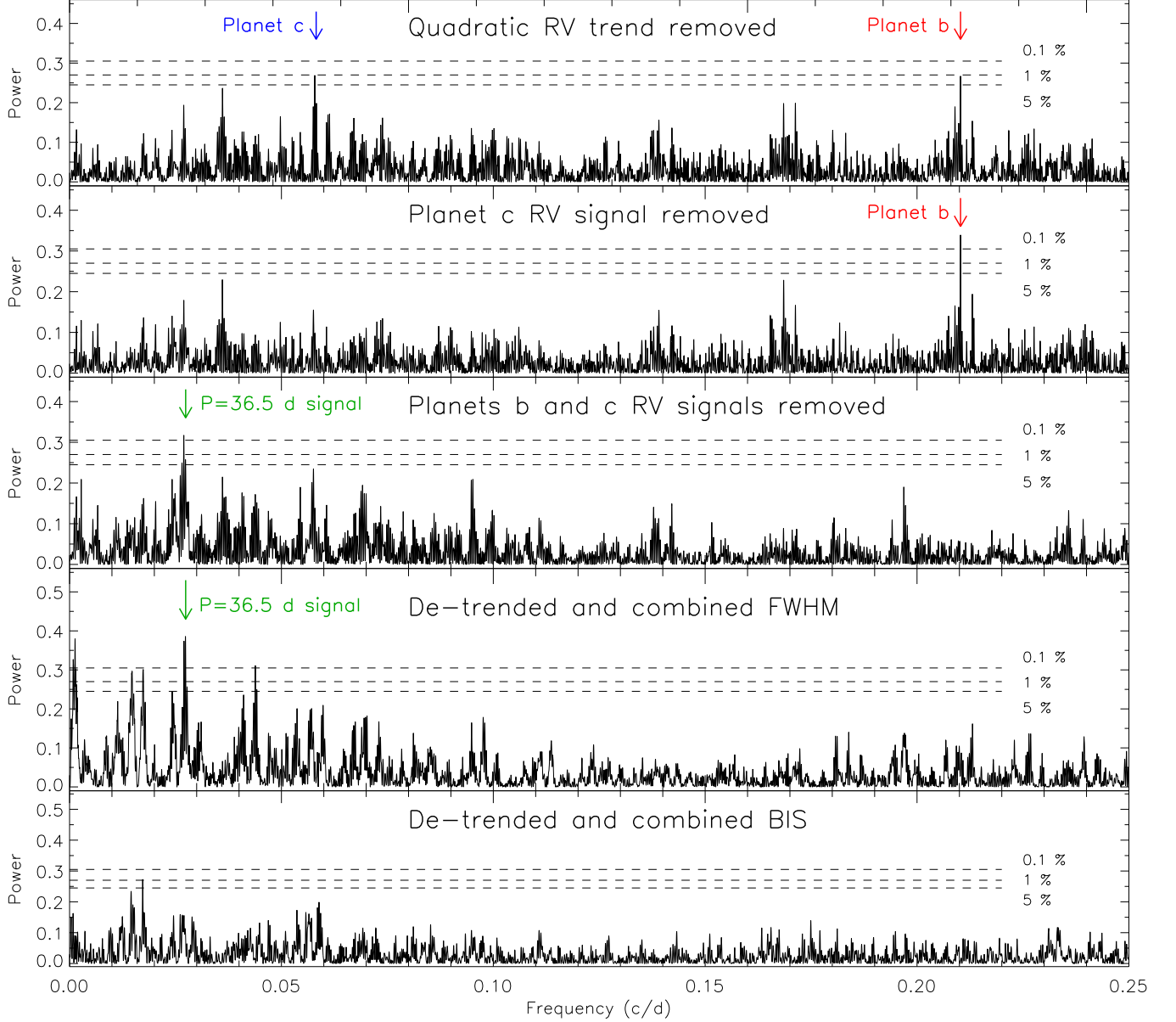


Figure 5. Generalized Lomb–Scargle periodograms of (1) the combined HARPS RV measurements, following the subtraction of the quadratic trend (first panel); (2) the RV residuals after subtracting the signal of HD 15337 c (second panel); (3) the RV residuals after subtracting the signal of HD 15337 b and c (third panel); (4) the FWHM of the cross-correlation function (fourth panel); (5) the bisector span (BIS) of the cross-correlation function (fifth panel). The dashed horizontal lines mark the FAP at 0.1%, 1% and 5 %. The frequencies of the two transiting planets, as well as of the signal at 36.5 days are marked with vertical arrows.

bisector span (BIS; lower panel). The generalized Lomb–Scargle (GLS) periodogram (Zechmeister & Kürster 2009) of the combined RV data shows significant power at frequencies lower than the inverse of the temporal baseline of the HARPS observations, which is visible as a quadratic trend in the upper panel of Fig. 4. A similar trend is observed in the FWHM obtained with the old fiber bundle (middle panel, blue circles), suggesting that the RV trend might be due to long-term stellar variabil-

ity (e.g., magnetic cycles)⁵. Alternatively, the RV trend might be induced by a long period orbiting companion, while the long-term variation of the FWHM might be ascribable to the steady instrument de-focusing observed between 2004 and 2015 (Lo Curto et al. 2015).

⁵ We note that the FWHM and BIS offsets between the two instrument set-ups are unknown.

The upper panel of Fig. 5 shows the GLS periodogram of the combined HARPS RVs, following the subtraction of the best-fitting quadratic trend (cfr. Fig. 4). The peaks with the highest power are found at the orbital frequencies of the two transiting planets ($f_c = 0.058$ c/d and $f_b = 0.210$ c/d), with false-alarm probabilities⁶ (FAPs) of $\approx 1\%$ and RV semi-amplitude of about $2.0\text{--}2.5\text{ ms}^{-1}$. The periodogram of the RV residuals after subtracting the signal of the outer planet (Fig. 5, second panel), shows a significant peak (FAP $< 0.1\%$) at the frequency of the inner planet. The two peaks have no counterparts in the periodograms of the activity indicators⁷ (FWHM and BIS; Fig. 5, fourth and fifth panels), suggesting that the signals are induced by two orbiting planets with periods of 4.8 and 17.2 days. Finally, the GLS periodogram of the RV residuals after subtracting the quadratic trend and the signals of the two planets (Fig. 5, third panel) displays a peak with a FAP $< 0.1\%$ at ~ 36.5 days, which is also significantly detected in the periodogram of the FWHM (fourth panel). We interpreted the 36.5 days signal as the rotation period of the star, which agrees with the value expected from the R'_{HK} activity indicator (Sect. 4.2).

6. JOINT ANALYSIS

We performed a joint analysis of the *TESS* light curve (Sect. 2) and RV measurements (Sect. 3) using the software suite *pyaneti*, which allows for parameter estimation from posterior distributions calculated using Markov chain Monte Carlo (MCMC) methods.

We removed stellar variability from the *TESS* light curves using a cubic spline with knots spaced every 1.5 days. We then extracted ~ 8 hours of *TESS* photometry centered on each of the nine (HD 15337 b) and three (HD 15337 c) transits observed by *TESS* during Sectors 3 and 4. As described in Sect. 3, we rejected two HARPS RVs and used the remaining 85 Doppler measurements, while accounting for an RV offset between the two different HARPS set-ups.

The RV model includes a linear and a quadratic term, to account for the long-term variation described in Sect. 5, as well as two Keplerians, to account for the Doppler reflex motion induced by HD 15337 b and HD 15337 c. The RV stellar signal at the star’s rotation period was modeled as an additional coherent sine-like curve whose period was constrained with a uniform

prior centered at $P_{\text{rot}} = 36.5$ days and having a width of 0.2 day, as derived from the FWHM of the peak detected in the periodogram of the HARPS FWHMs. For the phase and amplitude of the activity signal we adopted uniform priors. While this simple model might not fully reproduce the periodic and quasi-periodic variations induced by evolving active regions carried around by stellar rotation, it has proven to be effective in accounting for the stellar signal of active and moderately active stars (e.g., Pepe et al. 2013; Gandolfi et al. 2017; Barragán et al. 2018; Prieto-Arranz et al. 2018). Any variation not properly modeled by the coherent sine-curve, and/or any instrumental noise not included in the nominal RV uncertainties, were accounted for by fitting two RV jitter terms for the two HARPS set-ups.

We modeled the *TESS* transit light curves using the limb-darkened quadratic model of Mandel & Agol (2002). For the limb-darkening coefficients, we set Gaussian priors using the values derived by Claret (2017) for the *TESS* passband. We imposed conservative error bars of 0.1 on both the linear and quadratic limb-darkening terms. For the eccentricity and argument of periastron we adopted the parametrization proposed by Anderson et al. (2011). A preliminary analysis showed that the transit light curve poorly constrains the scaled semi-major axis (a/R_*). We therefore set a Gaussian prior on a/R_* using *Kepler*’s third law, the orbital period, and the derived stellar mass and radius (Sect. 4.2). We imposed uniform priors for the remaining fitted parameters. Details of the fitted parameters and prior ranges are given in Table 2. We used 500 independent Markov chains initialized randomly inside the prior ranges. Once all chains converged, we used the last 5000 iterations and saved the chain states every 10 iterations. This approach generates a posterior distribution of 250,000 points for each fitted parameter. Table 2 lists the inferred planetary parameters. They are defined as the median and 68% region of the credible interval of the posterior distributions for each fitted parameter. The transit and RV curves are shown in Fig. 6 and Fig. 7, along with the best-fitting models.

We also experimented with Gaussian Processes (GPs) to model the correlated RV noise associated with stellar activity. GPs model stochastic processes with a parametric description of the covariance matrix. GP regression has proven to be successful in modeling the effect of stellar activity for several other exoplanetary systems (see, e.g., Haywood et al. 2014; Grunblatt et al. 2015; López-Morales et al. 2016; Barragán et al. 2018). To this aim, we modified the code *pyaneti* in order to include a GP algorithm coupled to the MCMC method. We implemented the GP approach proposed by Rajpaul

⁶ The FAP was derived using the bootstrap method described in (Kuerster et al. 1997).

⁷ We combined the activity indicators from the two HARPS fibers by subtracting the best-fitting second-order polynomials shown in Fig. 4.

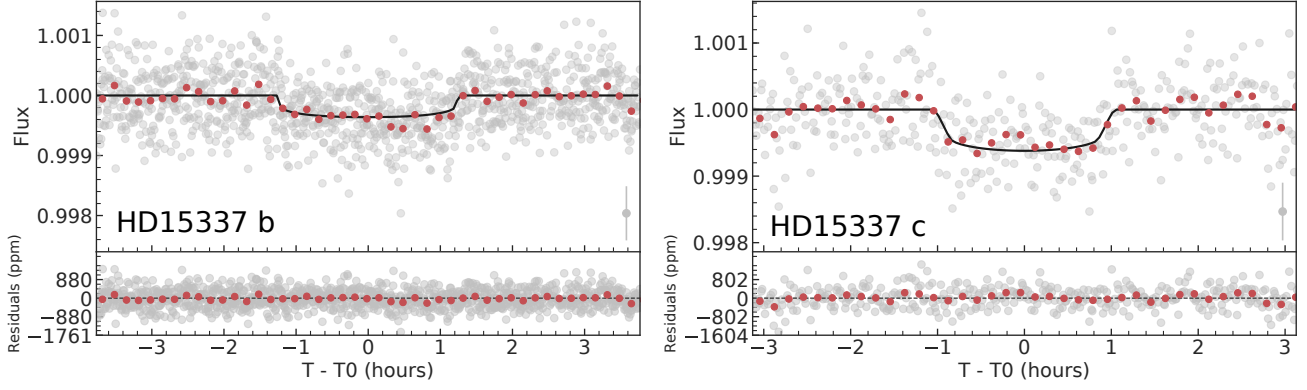


Figure 6. Folded transit light curves of HD 15337 b (left panel) and HD 15337 c (middle panel), based on nice and three single transits observed by *TESS*. The best-fitting transit models are overplotted with thick black lines. The *TESS* data points are shown with gray circles, whereas the 10 minutes binned data are displayed with red circles.

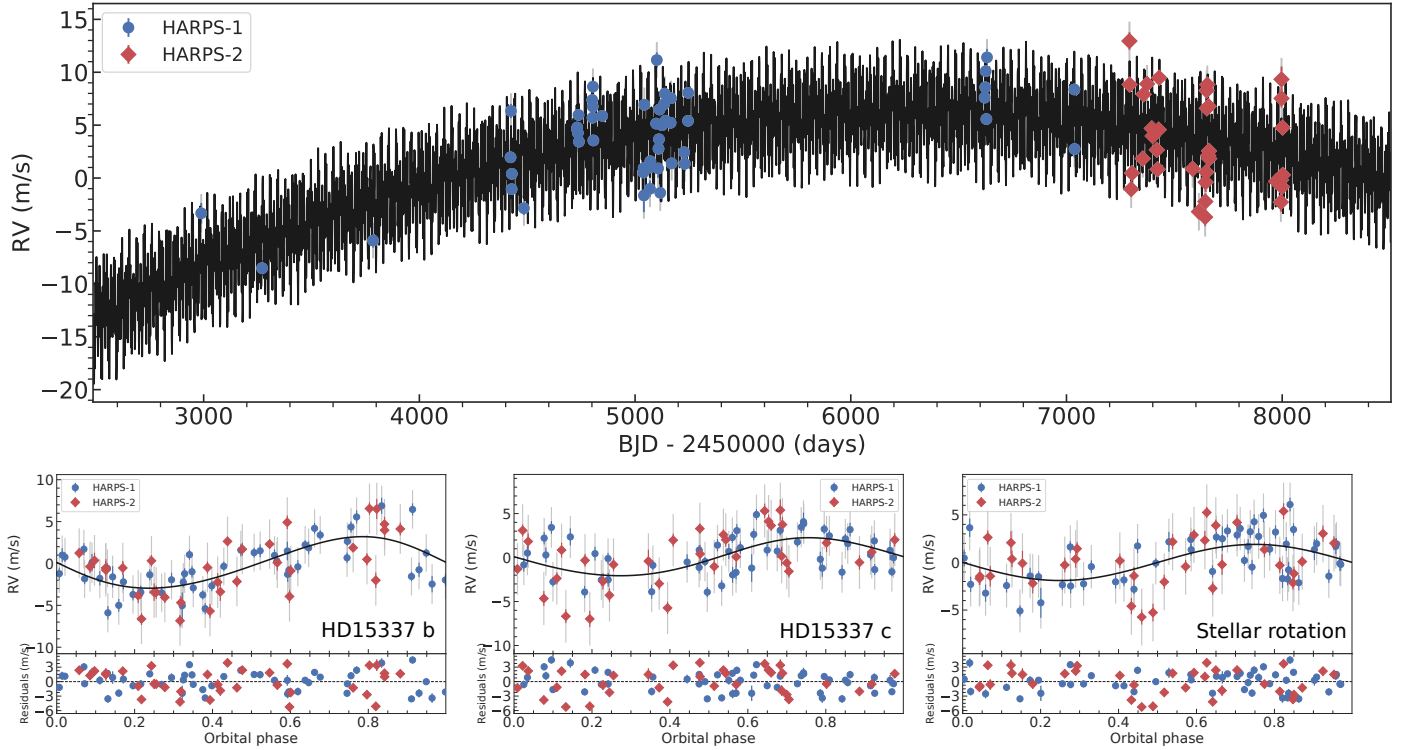


Figure 7. Upper panel: HARPS RV measurements vs. time, following the subtraction of the systemic velocities derived for the old (blue circles) and new (red diamonds) instrument set-up. Lower panels: phase-folded RV curves of HD 15337 b (left), HD 15337 c (middle) and stellar signal at 36.5 days (right). The best-fitting Keplerian and sine models are overplotted with thick black lines. The vertical gray lines mark the error bars including the RV jitter.

et al. (2015). Briefly, this framework assumes that the star-induced RV variations and activity indicators can be modeled by the same underlying GP and its derivative. This allows the GP to disentangle the RV activity component from the planetary signals.

We assumed that the stellar activity can be modeled by the quasi-periodic kernel described by Rajpaul et al. (2015). We modeled together the HARPS RV, BIS, and

FWHM time-series and we treated RV and BIS as being described by the GP and its first derivative, while for FWHM we assumed that it is only described by the GP. The fitted hyper-parameters are then V_c , V_r , B_c , B_r , L_c , as defined by Rajpaul et al. (2015), to account for the GP amplitudes of the RV, BIS, and FWHM signals, the period of the activity signal P_{GP} , the inverse of the harmonic complexity λ_p , and the long term evolution

timescale λ_e . We coupled this GP approach with the joint modeling described in the previous paragraphs of the present section (omitting the extra coherent signal).

As for the planetary signals, we imposed the same priors listed in Table 2. For the hyper-parameters, we used uniform priors, except for P_{GP} , for which we imposed a Gaussian prior with mean 36.5 days and standard deviation of 0.2 day. We used 250 chains to explore the parameter space. We created the posterior distributions with 500 iterations of converged chains, which generated a posterior distribution with 250,000 points for each parameters.

For planets b and c we derived an RV semi-amplitude of $2.71^{+0.54}_{-0.51}$ m s $^{-1}$ and $2.06^{+0.64}_{-0.58}$ m s $^{-1}$, respectively, which are in very good agreement with the values reported in Table 2. The other planetary and orbital parameters are also consistent with the values presented in Table 2. For the GP hyper-parameters, we found $V_c = 0.55 \pm 0.23$ m s $^{-1}$, $V_r = 70^{+27}_{-21}$ m s $^{-1}$, $B_c = 9.4^{+3.4}_{-2.9}$ m s $^{-1}$, $B_r = 64^{+20}_{-25}$ m s $^{-1}$, $L_c = 5.4 \pm 2.2$ m s $^{-1}$, $P_{GP} = 36.5 \pm 0.2$ d, $\lambda_e = 4217^{+624}_{-685}$ d, and $\lambda_p = 1086^{+501}_{-394}$. The relatively large values of the scale parameters in the GP, i.e. λ_e and λ_p , indicate that the stellar activity behaves like a sinusoidal signal (with slight corrections).

7. DISCUSSION AND CONCLUSIONS

The innermost transiting planet HD 15337 b ($P_{orb,b} = 4.8$ days) has a mass of $M_b = 7.51^{+1.09}_{-1.01} M_\oplus$ and a radius of $R_b = 1.64 \pm 0.06 R_\oplus$, yielding a mean density of $\rho_b = 9.30^{+1.81}_{-1.58}$ g cm $^{-3}$. Figure 8 displays the position of HD 15337 b on the mass-radius diagram compared to the sub-sample of small transiting planets ($R_p \leq 3 R_\oplus$) whose masses and radii have been derived with a precision better than 25%. Theoretical models from Zeng et al. (2016) are overplotted using different lines and colors. Given the precision of our mass determination ($\sim 14\%$), we conclude that HD 15337 b is a rocky terrestrial planet with a composition consisting of $\sim 50\%$ silicate and $\sim 50\%$ iron.

For HD 15337 c ($P_{orb,c} = 17.2$ days), we obtained a mass of $M_c = 8.11^{+1.82}_{-1.69} M_\oplus$ and a radius of $R_c = 2.39 \pm 0.12 R_\oplus$, yielding a mean density of $\rho_c = 3.23^{+0.90}_{-0.72}$ g cm $^{-3}$. Therefore, HD 15337 b and c have similar masses, but the radius of HD 15337 c is ~ 1.5 times larger than the radius of HD 15337 b. The lower bulk density of HD 15337 c suggests that the planet is likely composed by a rocky core surrounded either by a considerable amount of water, or by a light, hydrogen-dominated envelope. In the case of a water-rich planet, the amount of water and high planetary equilibrium temperature would imply the presence of a steam atmosphere, which would be strongly hydrogen dominated in its upper layer, as a consequence of

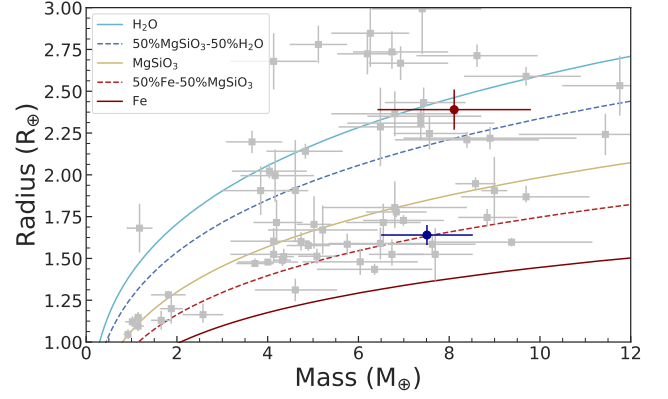


Figure 8. Mass-radius diagram for low-mass ($M_p < 12 M_\oplus$), small ($R_p < 3 R_\oplus$) planets with mass-radius measurements better than 25% (from <http://www.astro.keele.ac.uk/jkt/tepcat/>; Southworth 2011). Composition models from Zeng et al. (2016) are displayed with different lines and colors. The solid blue and red circles mark the position of HD 15337 b and HD 15337 c, respectively.

water dissociation and the low mass of hydrogen. It is therefore plausible to assume that HD 15337 c hosts a hydrogen-dominated atmosphere, at least in its upper part.

As in other systems hosting two close-in sub-Neptune-mass planets (e.g., HD 3167 Gandolfi et al. 2017), the radii of HD 15337 b and c lie on opposite sides of the radius gap (Fulton et al. 2017; Van Eylen et al. 2018), with the closer-in planet having a higher bulk density, similar to other close-in systems with measured planetary masses (e.g., HD 3167, K2-109, GJ 9827; Gandolfi et al. 2017; Guenther et al. 2017; Prieto-Arranz et al. 2018). This gap is believed to be caused by atmospheric escape (Owen & Wu 2017; Jin & Mordasini 2018), which is stronger for closer-in planets. Within this picture, HD 15337 b would probably have lost its primary, hydrogen-dominated atmosphere and now hosts a secondary atmosphere possibly resulting from out-gassing of a solidifying magma ocean, while HD 15337 c is likely to still partly retain the primordial hydrogen-dominated envelope. This is consistent with Van Eylen et al. (2018), who measured the location and slope of the radius gap as a function of orbital period and matched it to models suggesting a homogeneous terrestrial core composition.

To first order, the radii of HD 15337 b and c depend on the present-day properties of their atmospheres, which are intimately related to the amount of high-energy (X-ray and extreme ultraviolet; $\lambda < 91.2$ nm) stellar radiation received since the dispersal of the protoplanetary nebula, and thus also to the stellar rotation history. The evolution of the stellar rotation rate does not follow a unique path because stars of the same mass

and metallicity can have significantly different rotation rates up to about 1 Gyr (e.g., Mamajek & Hillenbrand 2008; Johnstone et al. 2015; Tu et al. 2015). For older stars, it is therefore not possible to infer their past high-energy emission from their measured stellar properties. Starting from the assumption that HD 15337 c hosted a hydrogen-dominated atmosphere with solar metallicity throughout its entire evolution, we derived the history of the stellar rotation and high-energy emission by modeling the atmospheric evolution of HD 15337 c. To this end, we employed the atmospheric evolution algorithm described by Kubyshkina et al. (2018) and further developed by Kubyshkina et al. (2019, ApJ, in press), which is based on a Bayesian approach, fitting the currently observed planetary radius and combining the planetary evolution model with the MCMC open-source algorithm of Cubillos et al. (2017). The planetary atmospheric evolution model, system parameters (i.e., planetary mass, planetary radius, orbital separation, current stellar rotation period, stellar age, stellar mass; Table 2) were then used to compute the posterior distribution for the stellar rotation rate at any given age via MCMC. We assumed Gaussian priors determined by the measured system parameters and their uncertainties.

Figure 9 shows the obtained posterior distribution for the rotation period HD 15337 at an age of 150 Myr in comparison with the distribution derived from measurements of open cluster stars of the same age (Johnstone et al. 2015). Our results indicate that HD 15337, when it was young, was likely to be a moderate rotator, with a high-energy emission at 150 Myr ranging between 3.7 and 127 times the current solar emission, further excluding that the star was a very fast/slow rotator. We further employed the result shown in Fig. 9 to estimate the past atmospheric evolution of a possible hydrogen-dominated atmosphere of HD 15337 b. Accounting for all uncertainties on the system parameters and on the derived history of the stellar rotation period, we obtained that HD 15337 b has completely lost its primary atmosphere, assuming it held one, within 300 Myr, in agreement with the currently observed mean density.

The position of HD 15337 c in the mass-radius diagram (Fig. 8) indicates that the planet may be hosting a massive hydrogen-dominated envelope or a smaller secondary atmosphere. As primary atmospheres are easily subject to escape, knowing the current composition of the envelope of HD 15337 c would provide a strong constraint on atmospheric evolution models. In this respect, this planet is similar to π Men c (Gandolfi et al. 2018; Huang et al. 2018); furthermore, as for π Men, the close distance to the system and brightness of the host star would enable high-quality transmission spec-

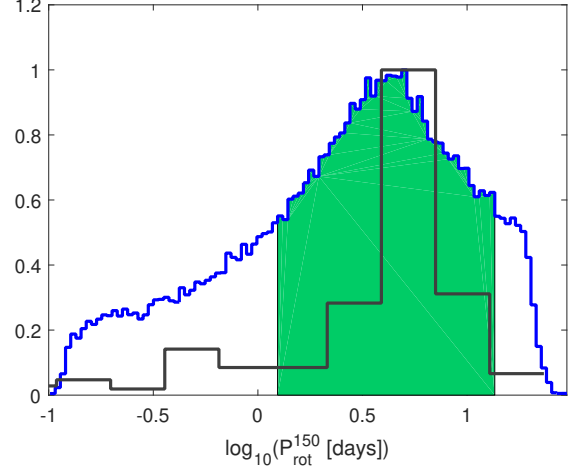


Figure 9. MCMC posterior distributions for the stellar rotation period at an age of 150 Myr obtained from the modeling of HD 15337 c. The shaded areas correspond to the 68% region of the credible interval of the posterior distribution. The black histogram shows the distribution of stellar rotation periods measured for open cluster stars with an age of 150 Myr (from Johnstone et al. 2015).

troscopy spanning from far-ultraviolet to infrared wavelengths. Of particular interest would be probes of an extended, escaping atmosphere. Spectral lines sensitive to various levels of extended atmospheres include H I, C II, and O I resonance lines in the ultraviolet, H α in the optical, and He I in the near-infrared. This suite of lines would provide a comprehensive picture of the upper atmosphere of the planet, thus constraining atmospheric escape and evolution models.

We are very grateful to the referee for a careful reading of this Letter and valuable suggestions and comments. We acknowledge the use of public *TESS* Alert data from pipelines at the *TESS* Science Office and at the *TESS* Science Processing Operations Center. This Letter includes data collected by the *TESS* mission, which are publicly available from the Mikulski Archive for Space Telescopes (MAST). Resources supporting this work were provided by the NASA High-End Computing (HEC) Program through the NASA Advanced Supercomputing (NAS) Division at Ames Research Center for the production of the SPOC data products. Funding for the *TESS* mission is provided by NASA’s Science Mission directorate. Based on observations collected at the European Organization for Astronomical Research in the Southern Hemisphere under ESO programs 072.C-0488, 183.C-0972, 192.C-0852, 196.C-1006, and 198.C-0836. This research has made use of the services of the ESO Science Archive Facility.

Table 2. HD 15337 System Parameters.

Parameter	Prior ^(a)	Derived Value
Stellar Parameters		
Star mass M_* (M_\odot)	...	0.90 ± 0.03
Star radius R_* (R_\odot)	...	0.856 ± 0.017
Effective temperature T_{eff} (K)	...	5125 ± 50
Surface gravity ^(b) $\log g_*$ (cgs)	...	4.53 ± 0.02
Surface gravity ^(c) $\log g_*$ (cgs)	...	4.40 ± 0.10
Iron abundance [Fe/H] (dex)	...	0.15 ± 0.10
Sodium abundance [Na/H] (dex)	...	0.27 ± 0.09
Calcium abundance [Ca/H] (dex)	...	0.16 ± 0.05
Projected rotational velocity $v \sin i_*$ (km s^{-1})	...	1.0 ± 1.0
Age (Gyr)	...	5.1 ± 0.8
Interstellar extinction A_V	...	0.02 ± 0.02
Model Parameters of HD 15337 b		
Orbital period $P_{\text{orb, b}}$ (days)	$\mathcal{U}[4.7552, 4.7572]$	4.75615 ± 0.00017
Transit epoch $T_{0, \text{b}}$ (BJD _{TDB} - 2 450 000)	$\mathcal{U}[8411.4526, 8411.4706]$	$8411.46156^{+0.00094}_{-0.00119}$
Scaled semi-major axis a_b/R_*	$\mathcal{N}[13.11, 0.17]$	$13.11^{+0.16}_{-0.15}$
Planet-to-star radius ratio R_b/R_*	$\mathcal{U}[0, 0.1]$	$0.01761^{+0.00055}_{-0.00058}$
Impact parameter b_b	$\mathcal{U}[0, 1]$	$0.33^{+0.09}_{-0.14}$
$\sqrt{e_b} \sin \omega_{*, \text{b}}$	$\mathcal{U}[-1, 1]$	$0.22^{+0.09}_{-0.11}$
$\sqrt{e_b} \cos \omega_{*, \text{b}}$	$\mathcal{U}[-1, 1]$	$0.12^{+0.14}_{-0.18}$
RV semi-amplitude variation K_b (m s^{-1})	$\mathcal{U}[0, 10]$	$3.08^{+0.44}_{-0.41}$
Model Parameters of HD 15337 c		
Orbital period $P_{\text{orb, c}}$ (days)	$\mathcal{U}[17.1676, 17.1876]$	17.1784 ± 0.0016
Transit epoch $T_{0, \text{c}}$ (BJD _{TDB} - 2 450 000)	$\mathcal{U}[8414.5416, 8414.5616]$	8414.5501 ± 0.0015
Scaled semi-major axis a_c/R_*	$\mathcal{N}[31.68, 0.70]$	31.87 ± 0.70
Planet-to-star radius ratio R_c/R_*	$\mathcal{U}[0, 0.1]$	0.0256 ± 0.0011
Impact parameter b_c	$\mathcal{U}[0, 1]$	$0.87^{+0.01}_{-0.02}$
$\sqrt{e_c} \sin \omega_{*, \text{c}}$	$\mathcal{U}[-1, 1]$	$-0.08^{+0.16}_{-0.15}$
$\sqrt{e_c} \cos \omega_{*, \text{c}}$	$\mathcal{U}[-1, 1]$	$0.12^{+0.15}_{-0.17}$
RV semi-amplitude variation K_c (m s^{-1})	$\mathcal{U}[0, 10]$	$2.16^{+0.48}_{-0.45}$
Additional Model Parameters		
Parameterized limb-darkening coefficient q_1	$\mathcal{N}[0.43, 0.1]$	0.37 ± 0.08
Parameterized limb-darkening coefficient q_2	$\mathcal{N}[0.19, 0.1]$	0.25 ± 0.11
Systemic velocity γ_{HS1} (km s^{-1})	$\mathcal{U}[-4.0, -3.6]$	-3.8174 ± 0.0027
Systemic velocity γ_{HS2} (km s^{-1})	$\mathcal{U}[-4.0, -3.6]$	-3.7977 ± 0.0012
RV jitter term σ_{HS1} (m s^{-1})	$\mathcal{U}[0, 100]$	$2.19^{+0.36}_{-0.30}$
RV jitter term σ_{HS2} (m s^{-1})	$\mathcal{U}[0, 100]$	$2.89^{+0.58}_{-0.43}$
Stellar rotation period (P_{rot}) days	$\mathcal{U}[36.4, 36.6]$	36.528 ± 0.022
Linear RV term $\text{m s}^{-1} \text{d}^{-1}$	$\mathcal{U}[-0.1, 0.1]$	-0.0057×0.0017
Quadratic RV term $\text{m s}^{-1} \text{d}^{-1}$	$\mathcal{U}[-0.1, 0.1]$	$-13.3 \pm 2.6 \times 10^{-7}$
Derived Parameters of HD 15337 b		
Planet mass M_b (M_\oplus)	...	$7.51^{+1.09}_{-1.01}$
Planet radius R_b (R_\oplus)	...	1.64 ± 0.06
Planet mean density ρ_b (g cm^{-3})	...	$9.30^{+1.81}_{-1.58}$
Semi-major axis of the planetary orbit a_b (au)	...	0.0522 ± 0.0012
Orbit eccentricity e_b	...	0.09 ± 0.05
Argument of periastron of stellar orbit $\omega_{*, \text{b}}$ (deg)	...	62^{+42}_{-32}
Orbit inclination i_b (deg)	...	$88.5^{+0.6}_{-0.4}$
Equilibrium temperature ^(d) $T_{\text{eq, b}}$ (K)	...	1001 ± 11.5
Transit duration $\tau_{14, \text{b}}$ (hr)	...	2.49 ± 0.06
Derived Parameters of HD 15337 c		
Planet mass M_c (M_\oplus)	...	$8.11^{+1.82}_{-1.69}$
Planet radius R_c (R_\oplus)	...	2.39 ± 0.12
Planet mean density ρ_c (g cm^{-3})	...	$3.23^{+0.90}_{-0.72}$
Semi-major axis of the planetary orbit a_c (au)	...	0.1268 ± 0.0038
Orbit eccentricity e_c	...	$0.05^{+0.06}_{-0.04}$
Argument of periastron of stellar orbit $\omega_{*, \text{c}}$ (deg)	...	329^{+69}_{-64}
Orbit inclination i_c (deg)	...	$88.5^{+0.2}_{-0.1}$
Equilibrium temperature ^(d) $T_{\text{eq, c}}$ (K)	...	642 ± 10
Transit duration $\tau_{14, \text{c}}$ (hr)	...	$2.25^{+0.20}_{-0.11}$

NOTE—(a) $\mathcal{U}[a, b]$ refers to uniform priors between a and b ; $\mathcal{N}[a, b]$ to Gaussian priors with mean a and standard deviation b ; (b)

Table 3. HARPS RV measurements of HD 15337 acquired with the old fiber bundle.

BJD _{TDB} ^a -2450000	RV (km s ⁻¹)	$\pm\sigma$ (km s ⁻¹)	BIS (km s ⁻¹)	FWHM (km s ⁻¹)	T _{exp} (s)	S/N ^b
2988.663700	-3.8208	0.0010	0.0013	6.1330	900	70.8
3270.822311	-3.8260	0.0008	0.0015	6.1353	900	93.7
3785.541537	-3.8234	0.0007	0.0010	6.1471	900	101.7
4422.673842	-3.8155	0.0006	0.0059	6.1571	900	108.1
4424.646720	-3.8111	0.0007	0.0037	6.1531	900	97.7
4427.703292	-3.8185	0.0006	0.0049	6.1547	900	101.4
4428.644416	-3.8170	0.0005	0.0034	6.1481	900	125.8
4484.550086	-3.8203	0.0006	0.0063	6.1631	900	102.6
4730.822010	-3.8128	0.0006	0.0100	6.1779	900	108.1
4731.764597	-3.8127	0.0007	0.0133	6.1767	900	98.8
4734.786220	-3.8132	0.0010	0.0150	6.1661	900	68.4
4737.774983	-3.8115	0.0011	0.0053	6.1684	900	62.2
4739.782074	-3.8140	0.0008	0.0015	6.1633	1200	79.4
4801.645505	-3.8101	0.0006	0.0061	6.1753	900	112.5
4802.681221	-3.8117	0.0007	0.0065	6.1745	900	100.7
4803.585301	-3.8107	0.0006	0.0078	6.1681	900	117.0
4804.621351	-3.8088	0.0008	0.0102	6.1717	900	85.6
4806.641716	-3.8139	0.0006	0.0078	6.1734	900	103.1
4847.567925	-3.8116	0.0006	0.0062	6.1635	900	113.6
5038.928157	-3.8169	0.0006	0.0088	6.1583	900	113.4
5039.878459	-3.8165	0.0009	0.0028	6.1577	900	78.1
5040.884957	-3.8191	0.0016	-0.0011	6.1644	900	47.0
5042.901725	-3.8105	0.0005	0.0036	6.1476	900	120.8
5067.879903	-3.8164	0.0007	0.0068	6.1558	900	93.6
5068.916098	-3.8185	0.0008	0.0056	6.1655	800	85.2
5070.833766	-3.8159	0.0008	0.0071	6.1630	900	84.5
5097.828049	-3.8123	0.0008	0.0012	6.1615	900	79.2
5100.771149	-3.8063	0.0007	0.0049	6.1668	900	91.2
5106.752698	-3.8165	0.0009	0.0080	6.1621	900	76.6
5108.758136	-3.8147	0.0009	0.0105	6.1507	900	73.4
5110.725697	-3.8138	0.0007	0.0023	6.1464	900	89.9
5113.727962	-3.8110	0.0006	0.0041	6.1508	900	116.6
5116.732322	-3.8188	0.0008	0.0028	6.1553	900	85.7
5124.719074	-3.8125	0.0005	0.0052	6.1507	900	126.2
5134.807289	-3.8104	0.0007	0.0066	6.1632	900	94.7
5137.624046	-3.8095	0.0006	0.0115	6.1656	900	102.7
5141.642265	-3.8120	0.0006	0.0095	6.1629	900	111.4
5164.557710	-3.8122	0.0006	0.0038	6.1587	900	104.4
5166.557368	-3.8099	0.0006	0.0008	6.1533	900	104.2
5169.552068	-3.8161	0.0005	0.0008	6.1593	900	120.8
5227.530636	-3.8150	0.0007	0.0091	6.1510	900	98.7
5230.529883	-3.8161	0.0007	-0.0025	6.1456	900	94.4
5245.518763	-3.8120	0.0007	0.0087	6.1559	900	97.8
5246.519846	-3.8169	0.0360	0.1136	6.3367	5	3.8
5246.526257	-3.8094	0.0007	0.0047	6.1576	900	94.9
6620.642369	-3.8098	0.0007	-0.0005	6.1539	1200	92.8
6623.580646	-3.8089	0.0010	0.0033	6.1612	900	69.8
6625.634172	-3.8073	0.0008	0.0024	6.1609	900	92.2
6628.589169	-3.8119	0.0013	0.0010	6.1674	900	58.4
6631.568567	-3.8060	0.0008	0.0040	6.1663	900	90.9
7036.603445	-3.8091	0.0009	0.0001	6.1772	900	83.9
7037.560130	-3.8147	0.0008	0.0041	6.1679	900	88.9

NOTE—(a) Barycentric Julian dates are given in barycentric dynamical time; (b) S/N per pixel at 550 nm; (*) outlier not included in the analysis.

Table 4. HARPS RV measurements of HD 15337 acquired with the new fiber bundle.

BJD _{TDB} ^a -2450000	RV (km s ⁻¹)	$\pm\sigma$ (km s ⁻¹)	BIS (km s ⁻¹)	FWHM (km s ⁻¹)	T _{exp} (s)	S/N ^b
7291.826359	-3.7848	0.0008	0.0273	6.2102	900	88.1
7292.799439	-3.7889	0.0007	0.0246	6.2141	900	95.6
7299.843584	-3.7988	0.0007	0.0229	6.1968	900	106.2
7303.879389	-3.7973	0.0013	0.0184	6.1985	900	60.3
7353.698805	-3.7959	0.0008	0.0209	6.2081	900	97.6
7357.682828	-3.7898	0.0006	0.0239	6.2073	900	127.1
7373.685080	-3.7889	0.0007	0.0207	6.2064	900	99.5
7395.644348	-3.7931	0.0011	0.0253	6.2093	900	68.5
7399.617257	-3.7938	0.0008	0.0213	6.1981	900	90.1
7418.584180	-3.7951	0.0007	0.0267	6.1927	900	108.5
7422.589672	-3.7969	0.0008	0.0211	6.1964	900	103.2
7427.538475	-3.7932	0.0008	0.0197	6.1990	900	94.5
7429.539077	-3.7883	0.0006	0.0222	6.2054	900	129.3
7584.927622	-3.7969	0.0007	0.0218	6.2010	900	97.2
7613.935104	-3.8009	0.0007	0.0214	6.1960	900	104.8
7641.794439	-1.6179	0.0009	0.0220	6.1919	900	81.4
7642.837840	-3.8015	0.0009	0.0196	6.1934	900	80.2
7643.808690	-3.8000	0.0008	0.0189	6.1928	900	89.1
7644.862657	-3.7982	0.0009	0.0202	6.1907	900	79.1
7647.923051	-3.7972	0.0007	0.0181	6.1888	900	110.7
7649.726575	-3.7895	0.0010	0.0205	6.1981	900	72.2
7650.752860	-3.7912	0.0006	0.0207	6.2017	900	115.2
7652.744706	-3.7889	0.0008	0.0222	6.1982	900	91.5
7656.751475	-3.7956	0.0008	0.0254	6.2022	900	87.1
7658.854305	-3.7910	0.0005	0.0196	6.1970	900	142.1
7660.797461	-3.7952	0.0008	0.0195	6.1985	900	85.9
7661.831637	-3.7959	0.0007	0.0116	6.2990	900	107.0
7971.834240	-3.7981	0.0009	0.0219	6.1895	900	79.6
7993.916286	-3.8000	0.0009	0.0246	6.2071	900	84.7
7994.887034	-3.7979	0.0011	0.0250	6.2032	900	70.0
7996.829372	-3.7884	0.0012	0.0185	6.2004	900	64.2
7996.923718	-3.7902	0.0009	0.0238	6.1989	1500	89.6
7998.866747	-3.7986	0.0010	0.0216	6.2004	900	72.2
8001.872927	-3.7930	0.0008	0.0188	6.1873	900	99.5
8002.895001	-3.7975	0.0009	0.0216	6.1880	900	82.8

NOTE—(a) Barycentric Julian dates are given in barycentric dynamical time; (b) S/N per pixel at 550 nm; (*) outlier not included in the analysis.

L.F. and D.K. acknowledge the Austrian Forschungsförderungsgesellschaft FFG project “TAPAS4CHEOPS” P853993. J.H.L. acknowledges the support of the Japan Society for the Promotion of Science (JSPS) Research Fellowship for Young Scientists. J.K., S.G., M.P., S.C., K.W.F.L., H.R., A.H., and M.E. acknowledge the support by DFG Grants PA525/18-1, PA525/19-1, PA525/20-1, HA 3279/12-1 and RA 714/14-1 within the DFG Priority Program SPP1992: “Exploring the Diversity of Exoplanets.” H.J.D. and D.N. acknowledge support by grants ESP2015-65712-C5-4-R, ESP2016-80435-C2-2-R, and ESP2017-87676-C5-4-R of the Spanish Secretary of State for R&D&i (MINECO). S.C. thanks the Hungarian National Research, Development and Innovation Office for the NKFI-KH-130372 grant. SM acknowledges support from the Ramon y Cajal fellowship number RYC-2015-17697. This work is partly sup-

ported by JSPS KAKENHI grant Nos. JP18H01265 and 18H05439, and JST PRESTO grant No. JPMJPR1775. I.R. acknowledges support from the Spanish Ministry for Science, Innovation and Universities (MCIU) and the Fondo Europeo de Desarrollo Regional (FEDER) through grant ESP2016-80435-C2-1-R, as well as the support of the Generalitat de Catalunya/CERCA programme. M.F. and C.M.P. gratefully acknowledge the support of the Swedish National Space Agency. 17-01752J. M.S. acknowledges the Postdoc@MUNI project CZ.02.2.69/0.0/0.0/16-027/0008360.

Facilities: TESS, HARPS

Software: VARLET (Grziwa & Pätzold 2016), PHALET (Grziwa & Pätzold 2016), SME (Valenti & Piskunov 1996; Valenti & Fischer 2005; Piskunov & Valenti 2017), pyaneti (Barragán et al. 2019)

REFERENCES

- Alibert, Y., & Benz, W. 2017, *A&A*, 598, L5
- Alibert, Y., Mousis, O., Mordasini, C., & Benz, W. 2005, *ApJL*, 626, L57
- Anderson, D. R., Collier Cameron, A., Hellier, C., et al. 2011, *ApJL*, 726, L19
- Axer, M., Fuhrmann, K., & Gehren, T. 1994, *A&A*, 291, 895
- Baranne, A., Queloz, D., Mayor, M., et al. 1996, *A&AS*, 119, 373
- Barragán, O., Gandolfi, D., & Antoniciello, G. 2019, *MNRAS*, 482, 1017
- Barragán, O., Gandolfi, D., Dai, F., et al. 2018, *A&A*, 612, A95
- Bianchi, L., Herald, J., Efremova, B., et al. 2011, *Ap&SS*, 335, 161
- Bruntt, H., Bedding, T. R., Quirion, P.-O., et al. 2010, *MNRAS*, 405, 1907
- Castelli, F., & Kurucz, R. L. 2003, in *IAU Symposium*, Vol. 210, *Modelling of Stellar Atmospheres*, ed. N. Piskunov, W. W. Weiss, & D. F. Gray, A20
- Christiansen, J. L., Jenkins, J. M., Caldwell, D. A., et al. 2012, *PASP*, 124, 1279
- Claret, A. 2017, *A&A*, 600, A30
- Cubillos, P., Harrington, J., Lored, T. J., et al. 2017, *AJ*, 153, 3
- Cutri, R. M., Skrutskie, M. F., van Dyk, S., et al. 2003, *2MASS All Sky Catalog of point sources*.
- Cutri, R. M. e. 2013, *VizieR Online Data Catalog*, 2328
- Doyle, A. P., Davies, G. R., Smalley, B., Chaplin, W. J., & Elsworth, Y. 2014, *MNRAS*, 444, 3592
- Esposito, M., Armstrong, D. J., Gandolfi, D., et al. 2019, *A&A*, 623, A165
- Fuhrmann, K., Axer, M., & Gehren, T. 1993, *A&A*, 271, 451
- . 1994, *A&A*, 285, 585
- Fuhrmann, K., Pfeiffer, M., Frank, C., Reetz, J., & Gehren, T. 1997a, *A&A*, 323, 909
- Fuhrmann, K., Pfeiffer, M. J., & Bernkopf, J. 1997b, *A&A*, 326, 1081
- Fulton, B. J., Petigura, E. A., Howard, A. W., et al. 2017, *AJ*, 154, 109
- Gaia Collaboration, Brown, A. G. A., Vallenari, A., et al. 2018, *A&A*, 616, A1
- Gandolfi, D., Barragán, O., Hatzes, A. P., et al. 2017, *AJ*, 154, 123
- Gandolfi, D., Barragán, O., Livingston, J. H., et al. 2018, *A&A*, 619, L10
- Gomes da Silva, J., Santos, N. C., Boisse, I., Dumusque, X., & Lovis, C. 2014, *A&A*, 566, A66
- Grunblatt, S. K., Howard, A. W., & Haywood, R. D. 2015, *ApJ*, 808, 127
- Grziwa, S., & Pätzold, M. 2016, *ArXiv e-prints*, arXiv:1607.08417
- Guenther, E. W., Barragán, O., Dai, F., et al. 2017, *A&A*, 608, A93
- Gustafsson, B., Edvardsson, B., Eriksson, K., et al. 2008, *A&A*, 486, 951
- Haywood, R. D., Collier Cameron, A., Queloz, D., et al. 2014, *MNRAS*, 443, 2517

- Henden, A. A., Levine, S., Terrell, D., & Welch, D. L. 2015, in *American Astronomical Society Meeting Abstracts*, Vol. 225, American Astronomical Society Meeting Abstracts #225, 336.16
- Høg, E., Fabricius, C., Makarov, V. V., et al. 2000, *A&A*, 355, L27
- Huang, C. X., Burt, J., Vanderburg, A., et al. 2018, *ApJL*, 868, L39
- Jenkins, J. M., Twicken, J. D., McCauliff, S., et al. 2016, in *Proc. SPIE*, Vol. 9913, *Software and Cyberinfrastructure for Astronomy IV*, 99133E
- Jin, S., & Mordasini, C. 2018, *ApJ*, 853, 163
- Johnstone, C. P., Güdel, M., Brott, I., & Lüftinger, T. 2015, *A&A*, 577, A28
- Jones, M. I., Brahm, R., Espinoza, N., et al. 2018, *arXiv e-prints*, arXiv:1811.05518
- Kovács, G., Zucker, S., & Mazeh, T. 2002, *A&A*, 391, 369
- Kubyshkina, D., Fossati, L., Erkaev, N. V., et al. 2018, *A&A*, 619, A151
- Kuerster, M., Schmitt, J. H. M. M., Cutispoto, G., & Dennerl, K. 1997, *A&A*, 320, 831
- Lo Curto, G., Pepe, F., Avila, G., et al. 2015, *The Messenger*, 162, 9
- López-Morales, M., Haywood, R. D., Coughlin, J. L., et al. 2016, *AJ*, 152, 204
- Mamajek, E. E., & Hillenbrand, L. A. 2008, *ApJ*, 687, 1264
- Mandel, K., & Agol, E. 2002, *ApJL*, 580, L171
- Mayor, M., Pepe, F., Queloz, D., et al. 2003, *The Messenger*, 114, 20
- Nielsen, L. D., Bouchy, F., Turner, O., et al. 2019, *A&A*, 623, A100
- Owen, J. E., & Wu, Y. 2017, *ApJ*, 847, 29
- Paunzen, E. 2015, *A&A*, 580, A23
- Pepe, F., Cameron, A. C., Latham, D. W., et al. 2013, *Nature*, 503, 377
- Piskunov, N., & Valenti, J. A. 2017, *A&A*, 597, A16
- Prieto-Arranz, J., Palle, E., Gandolfi, D., et al. 2018, *A&A*, 618, A116
- Quinn, S. N., Becker, J. C., Rodriguez, J. E., et al. 2019, *arXiv e-prints*, arXiv:1901.09092
- Rajpaul, V., Aigrain, S., Osborne, M. A., Reece, S., & Roberts, S. 2015, *MNRAS*, 452, 2269
- Ricker, G. R., Winn, J. N., Vanderspek, R., et al. 2015, *Journal of Astronomical Telescopes, Instruments, and Systems*, 1, 014003
- Schlegel, D. J., Finkbeiner, D. P., & Davis, M. 1998, *ApJ*, 500, 525
- Smith, J. C., Stumpe, M. C., Van Cleve, J. E., et al. 2012, *Publications of the Astronomical Society of the Pacific*, 124, 1000
- Southworth, J. 2011, *MNRAS*, 417, 2166
- Spada, F., Demarque, P., Kim, Y.-C., & Sills, A. 2013, *ApJ*, 776, 87
- Stassun, K. G., Collins, K. A., & Gaudi, B. S. 2017, *AJ*, 153, 136
- Stassun, K. G., Corsaro, E., Pepper, J. A., & Gaudi, B. S. 2018a, *AJ*, 155, 22
- Stassun, K. G., & Torres, G. 2016, *AJ*, 152, 180
- . 2018, *ApJ*, 862, 61
- Stassun, K. G., Oelkers, R. J., Pepper, J., et al. 2018b, *AJ*, 156, 102
- Stumpe, M. C., Smith, J. C., Van Cleve, J. E., et al. 2012, *Publications of the Astronomical Society of the Pacific*, 124, 985
- Torres, G., Andersen, J., & Giménez, A. 2010, *A&A Rv*, 18, 67
- Trifonov, T., Rybizki, J., & Kürster, M. 2019, *A&A*, 622, L7
- Tu, L., Johnstone, C. P., Güdel, M., & Lammer, H. 2015, *A&A*, 577, L3
- Valenti, J. A., & Fischer, D. A. 2005, *ApJS*, 159, 141
- Valenti, J. A., & Piskunov, N. 1996, *A&AS*, 118, 595
- Van Eylen, V., Agentoft, C., Lundkvist, M. S., et al. 2018, *MNRAS*, 479, 4786
- Yi, S., Demarque, P., Kim, Y.-C., et al. 2001, *ApJS*, 136, 417
- Zechmeister, M., & Kürster, M. 2009, *A&A*, 496, 577
- Zeng, L., Sasselov, D. D., & Jacobsen, S. B. 2016, *ApJ*, 819, 127